This article is made available for a limited time sponsored by ACS under the ACS Free to Read License, which permits copying and redistribution of the article for non-commercial scholarly purposes.

ACS MATERIALS LETTERS

Cite This: ACS Materials Lett. 2020, 2, 20−27

www.acsmaterialslett.org

LETTER

Large Polaron Self-Trapped States in Three-Dimensional Metal-Halide Perovskites

Walter P. D. Wong,[†,▽] Jun Yin,[‡,▽] Bhumika Chaudhary,[§,∥] Xin Yu Chin,[∥] Daniele Cortecchia,[§,∥] Shu-Zee A. Lo,[⊥] Andrew C. Grimsdale,[†] Omar F. Mohammed,[‡] Guglielmo Lanzani,[∥,#,★] and Cesare Soci*[,∥,⊥]

[†]School of Materials Science and Engineering, Nanyang Technological University, 50 Nanyang Avenue, Singapore 639798

[‡]Division of Physical Science and Engineering, King Abdullah University of Science and Technology, Thuwal 23955-6900, Saudi Arabia

[§]Interdisciplinary Graduate School, Nanyang Technological University, 50 Nanyang Avenue, Singapore 639798

[∥]Energy Research Institute (ERI@N), Research Techno Plaza, X-Frontier Block, Level 5, 50 Nanyang Drive, Singapore 637553

[⊥]Division of Physics and Applied Physics, School of Physical and Mathematical Sciences, Nanyang Technological University, 21 Nanyang Link, Singapore, 637371

[#]Dipartimento di Fisica, Politecnico di Milano, Piazza Leonardo da Vinci 32, Milano, Italy

[★]CNST@PoliMi, Istituto Italiano di Tecnologia (IIT), Via Giovanni Pascoli 70/3, Milano, Italy

Supporting Information

ABSTRACT: **In recent years, metal halide perovskites have generated tremendous interest for optoelectronic applications and their underlying fundamental properties. Because of the large electron-phonon coupling characteristic of soft lattices, self-trapping phenomena are expected to dominate hybrid perovskite photoexcitation dynamics. Yet, while the photogeneration of small polarons was proven in low-dimensional perovskites, the nature of polaron excitations in technologically relevant 3D perovskites, and their influence on charge carrier transport, remain elusive. In this study, we used a combination of first principle calculations and advanced spectroscopy techniques spanning the entire optical frequency range to pin down polaron features in three-dimensional metal halide perovskites. Mid-infrared photoinduced absorption shows the photogeneration of states associated with low energy intragap electronic transitions with lifetime up to the millisecond time scale, and vibrational mode renormalization in both frequency and amplitude. Density functional theory supports the assignment of the spectroscopic features to large polarons leading to new intragap transitions, hardening of phonon mode frequency, and renormalization of the oscillator strength. Theory provides quantitative estimation for the charge carrier masses and mobilities increase upon polaron formation, confirming experimental results. Overall, this work contributes to complete the scenario of elementary photoexcitations in metal halide perovskites and highlights the importance of polaronic transport in perovskite-based optoelectronic devices.**

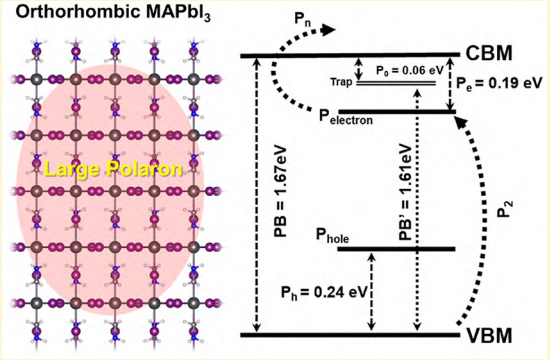

Metal halide perovskites (MHPs) are attracting enormous interest as solution-processed[1,2] active materials in a variety of device applications.[3−15] The prototype compound is methylammonium lead iodide ($MAPbI_3$), which is a three-dimensional (3D) hybrid perovskite known for its remarkable transport properties, such as long charge carrier lifetime[16] and diffusion length,[17−19] small nonradiative bimolecular recombination coefficient (γ) of the order of 10^{-10} cm^3 s^{-1}, comparable to those of crystalline semiconductors such as GaAs,[20,21] and apparent insensitivity to defects.[22−25] However, the nature of the charge carriers responsible for such remarkable performance is still under debate. Reported charge carrier mobilities in perovskite films between 10^{-4} and 10 cm^2 V^{-1} s^{-1}, depending on measurement technique,[16,17,20,26−30] are indeed in net contrast with the prediction of the Langevin model for free charge carrier recombination in semiconductors, where $\gamma/\mu = e/(\varepsilon_0\varepsilon_r)$.[27] The origin of such apparent inconsistency is still debated[31] and points toward the role of polaronic protection of charge carriers in the perovskite lattice.[32,33]

Received: July 17, 2019
Accepted: November 15, 2019
Published: November 15, 2019

© 2019 American Chemical Society

DOI: 10.1021/acsmaterialslett.9b00276
ACS Materials Lett. 2020, 2, 20−27

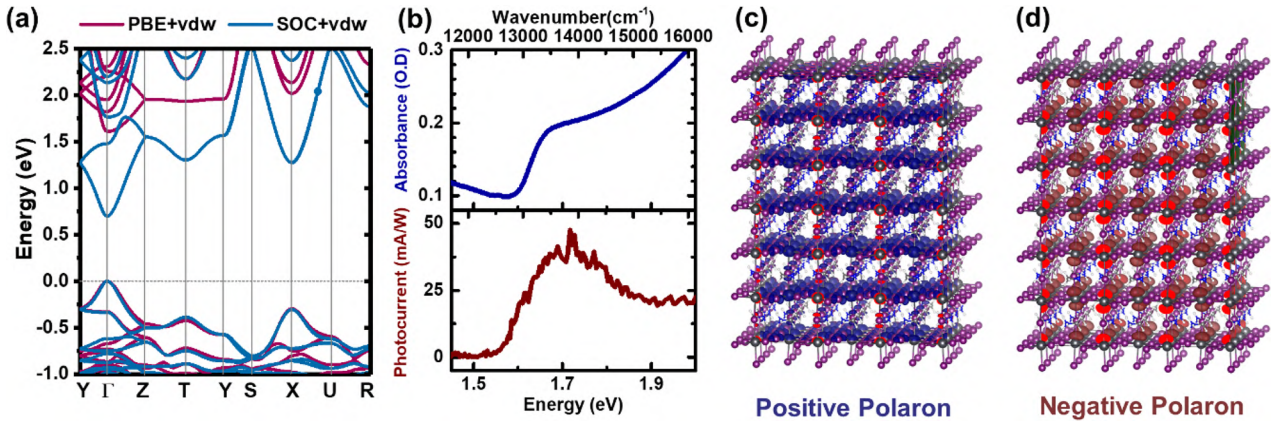

Figure 1. Electronic structure, absorption spectra, and photocurrent spectra of orthorhombic $MAPbI_3$. (a) Calculated band structures at GGA/PBE + vdw level without and with SOC effects; (b) linear absorption (top) and normalized steady-state photocurrent spectra obtained with illumination intensity of ~20 $\mu W/cm^2$ under applied field of 9 kV/cm (bottom); (c, d) electronic charge densities of positive polaronic states (panel (c)) and negative polaronic states (panel (d)) for a 3 × 3 × 3 supercell calculated at the GGA/PBE level.

Table 1. Calculated Effective Mass (m^*, × m_0) and Mobility ($cm^2\ V^{-1}\ s^{-1}$, Average of Different Crystallographic Directions) of Free Charges and Polarons in Tetragonal- and Orthorhombic-Phase $MAPbI_3$ (Including Spin-Orbit Coupling Effects)

	Tetragonal (300 K)			Orthorhombic (77 K)		
	Effective Mass			Effective Mass		
type	M(Y) → Γ	Γ → Z	mobility ($cm^2\ V^{-1}\ S^{-1}$)	M(Y) → Γ	Γ → Z	mobility ($cm^2\ V^{-1}\ S^{-1}$)
free hole	0.240	0.180	332.2	0.166	0.253	1491.6
positive polaron	1.411	1.058	215.4	0.976	1.487	497.9
free electron	0.220	0.107	630.5	0.121	0.204	5122.0
negative polaron	1.293	0.629	225.9	0.711	1.199	550.7

Because of the highly deformable and polar nature of the metal halide framework, MHPs are prone to lattice relaxation, which is expected to cause self-trapping of the elementary excitations into phonon-dressed localized states.[34−36] In low-dimensional perovskites (e.g., two-dimensional (2D) and one-dimensional (1D) structures), where Coulomb interactions are enhanced by reduced dielectric screening and quantum confinement effects, the formation of self-trapped excitons (*small polarons*) manifests itself in apparent radiative recombination effects, such as white-light emission in compounds such as (EDBE)$PbBr_4$.[35,37−39] Here, ab initio calculations have indicated that the excess charge is spatially confined to one crystal unit cell or less, inducing local distortions of the lead-halide framework. Photoexcitation in 2D perovskites gives rise to photoinduced lattice deformations[34,35,40] associated with polaron exciton states, with a characteristic fine structure in the absorption lineshapes.[41] On the other hand, for charge carriers in 3D perovskites,[42] because of the long-range electron phonon interaction typical of ionic crystals, polarons may extend over several lattice sites (*large polarons*). Large polarons can display bandlike coherent transport with a mobility of >1 $cm^2\ V^{-1}\ s^{-1}$, which decreases as the temperature increases.[33,43] In addition, the electrostatic screening brought about by the ionic (polar) lattice deformation could hinder Coulomb-mediated processes such as Auger cooling and Langevin recombination.[44]

Several recent works have postulated the existence of large polaron states in 3D MHPs. Among these are the electrical conductivity exhibiting characteristic power-law temperature dependence,[45] the steady-state photoinduced absorption (PIA) in the visible[46] and far-infrared (FIR) spectral range,[47] terahertz spectroscopic investigations,[48,49] and time-resolved optical Kerr effect spectroscopy (TR-OKE)[32] and optical absorption spectroscopy (TR-OAS).[50] Formation of long-lived energetic carriers with ~10^2 ps lifetime in $MAPbBr_3$ and $FAPbBr_3$ points toward the screening of charge carriers in the form of large polarons through liquidlike collective reorientation of the molecular dipoles.[51] Impulsive Raman scattering performed on $MAPbBr_3$[52] revealed the presence of coherent phonon modes generated via displacive excitation that is indicative of strong electron-phonon coupling, instrumental to polaron formation but not a proof of their existence. Similarly, a polaron state has been invoked to explain the octahedral distortion of $[PbI_6]^{4-}$ sustained by coherent vibrations of the Pb−I normal modes in $MAPbI_3$.[53] Nonetheless, the impact of carrier-induced lattice distortion on polaron formation and charge transport in optoelectronic devices has remained elusive.[16]

In this work, we identify the geometrical pattern associated with large self-trapped polaron states in $MAPbI_3$ by combining an advanced theoretical investigation of charge-induced lattice relaxation with the experimental study of specific vibrational modes. We assign the unique spectroscopic signatures in the infrared (IR) spectral region to the polaron-induced lattice relaxation and those in the near-infrared (NIR) to visible range to the polaron-induced electronic transitions. Based on this assignment, we further study polaron generation and long decay dynamics with femtosecond temporal resolution and present the first "real time" fast photocurrent transients, which directly measure charge carrier relaxation at the picosecond time scale and beyond. The correspondence between transient absorption and photocurrent decay kinetics supports the conjecture that polarons are primary charge carriers in 3D perovskites.

DOI: 10.1021/acsmaterialslett.9b00276
ACS Materials Lett. 2020, 2, 20−27

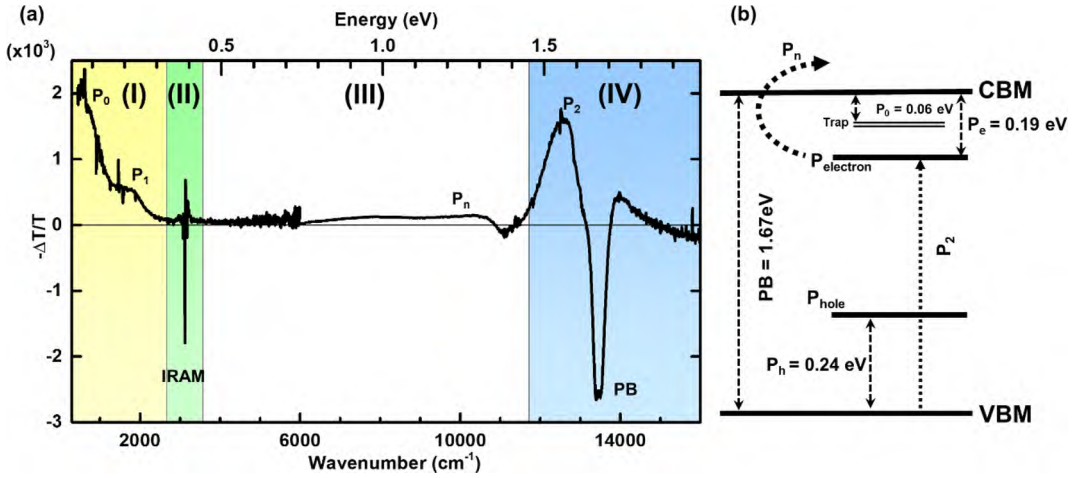

Figure 2. (a) cw-PIA spectrum of $MAPbI_3$. Region I (500−2600 cm^{-1}) shows the intragap polaron electronic transition P_1 = 0.20 eV and the trap state absorption P_0 = 0.06 eV, convoluted with infrared-active vibrational (IRAV) modes. Region II (2600−3500 cm^{-1}) shows infrared-active modulation (IRAM) of the C−H and N−H vibrational mode frequencies. Region III (3500−11700 cm^{-1}) indicates the presence of PIA transitions to higher lying states. Region IV (11700−16000 cm^{-1}) contains high-energy intragap polaron transitions and photobleaching (PB) of ground-state absorption. (b) Proposed electronic energy diagram and associated transitions, based on the calculated polaron state energies. P_1 is assigned to the convolution of positive polaron P_h = 0.24 eV and negative polaron P_e = 0.187 eV transitions above the valence band maximum (VBM) and below the conduction band minimum (CBM), respectively.

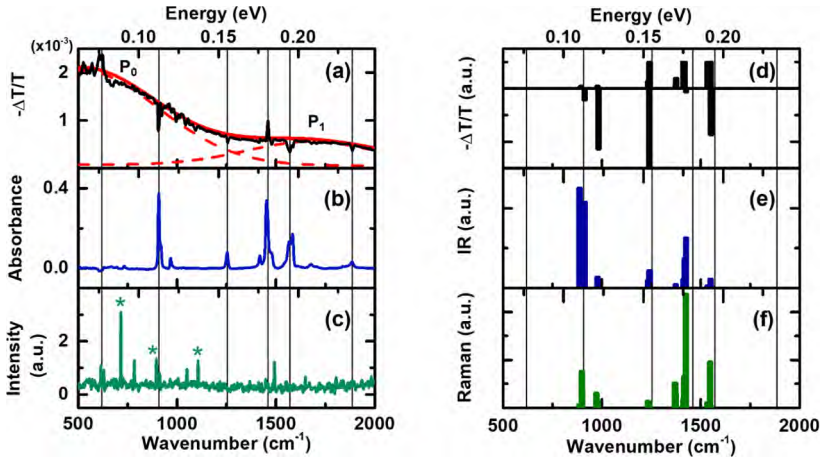

Figure 3. Experimental and simulated infrared active vibrational (IRAV) and Raman modes. (a) PIA spectrum (T = 78 K) fitted to two Gaussian peaks centered at ∼1650 cm^{-1} and 516 cm^{-1} (red dashed lines), (b) FTIR spectrum (T = 78 K), and (c) Raman spectrum (λ_{exc} = 1024 nm, T = 300 K), where green asterisks denote peaks from the CaF_2 substrate. (d) Simulated photoinduced absorption modes obtained as $-(\Delta T/T) = -(IR_{neut} - IR_{exc})/IR_{neut}$, where IR_{exc} and IR_{neut} are the IR mode intensities of excited and ground states, respectively. (e, f) Calculated IR and Raman mode intensity spectra of orthorhombic $MAPbI_3$. The main vibrational modes are indicated by black vertical lines, showing the correspondence between IRAV modes and Raman modes, which become IR-active under photoexcitation.

The band structure of orthorhombic-phase $MAPbI_3$ was calculated at GGA/PBE + vdW level without and with spin-orbit coupling (SOC) effects (Figure 1a). The resulting bandgap (1.61 eV, without SOC) is in good agreement with the experimental value deduced from the steady-state absorption spectra and the onset of steady-state photocurrent (Figure 1b). Inclusion of SOC in the band structure calculations considerably reduces the bandgap to 0.70 eV due to band splitting. As shown in Table 1, the extracted values of free carriers effective masses (m^*) along the M → Γ/Γ → Z directions are 0.166/0.253 (hole) and 0.121/0.204 (electron) for the low-temperature orthorhombic-phase $MAPbI_3$. The similar values obtained for hole and electron effective masses confirm the ambipolar nature of charge transport in $MAPbI_3$, while the different values for different crystallographic directions reflects the intrinsic anisotropy of the 3D perovskite lattice. Similar results are obtained for the high-temperature tetragonal phase, except for the inverted transport anisotropy.

Adding a positive/negative charge to the neutral lattice induces spontaneous structural relaxation of the supercell to a new equilibrium geometry, leading to the formation of positive and negative polarons (Figures 1c and 1d). The new half-filled energy level associated to the negative polaron lies 0.187 eV below the conduction band minimum (CBM), while that associated to the positive polaron lies 0.235 eV above the valence band maximum (VBM). The resulting charge density distributions suggest that the self-trapped polaron states are localized in spatially distinct regions within ∼2-3 inorganic atomic layers. Charge localization with comparable spatial extent was also observed in 3D and 2D perovskites when varying the Pb−I distances[35] or increasing the tilting of Pb−I−Pb angles.[32] Accordingly, the calculated polaronic effective

DOI: 10.1021/acsmaterialslett.9b00276
ACS Materials Lett. 2020, 2, 20−27

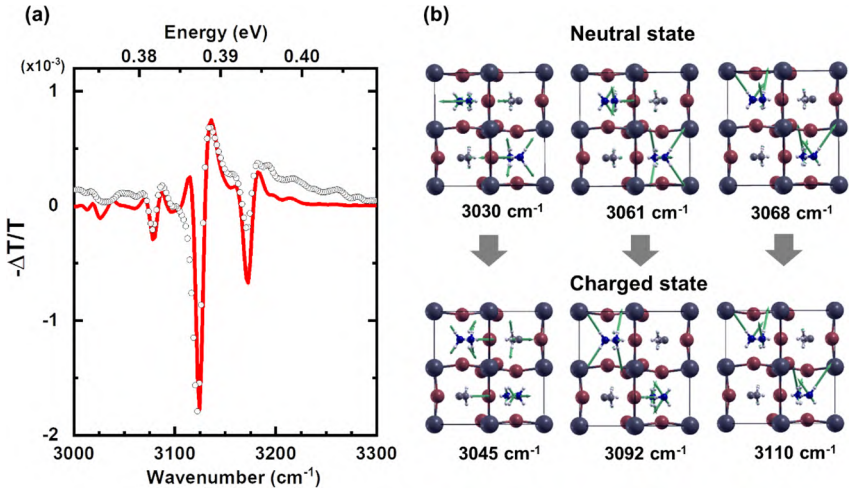

Figure 4. Infrared active modulation (IRAM) of C−H and N−H vibrational modes. (a) Experimental data fitted to a linear combination of first and second derivative of the IR absorption spectrum $f(\bar{\nu})$, $f_{der}(\bar{\nu}) = -0.0075f'(\bar{\nu}) + 0.1f''(\bar{\nu})$. The first derivative indicates a spectral shift of the absorption peak, while the second derivative indicates its spectral broadening; in this case, C−H and N−H mode hardening upon photoexcitation induces a blue shift of the vibrational modes. (b) Representative IR vibrational frequencies and displacement vectors obtained from phonon calculations, and corresponding blue-shift of IR-active-mode frequencies in the charged state.

masses in $MAPbI_3$ system are ∼5 times larger than those of free carriers and calculated polaron mobilities are 1.5−8 times smaller than free charge carrier mobilities.

The electronic and vibrational structure of semiconductors are strongly affected by polaron formation: (i) half-filled electronic states appear within the gap, giving rise to new optical transitions; (ii) vibrational mode frequencies are renormalized by the change in bond geometry, including modes of the inorganic lattice and of the organic moiety that "feel" a deformed environment (*spectator modes*),[51,53,54] but are not directly coupled to the carrier; and (iii) geometric distortion induces local symmetry breaking that relaxes vibrational selection rules and eventually activates vibrational modes that are silent for bare states. To test all these specific predictions, we measured the IR-photoinduced absorption of $MAPbI_3$ over a broad spectral range (Figure 2a).

Low-temperature ($T \approx 80$ K) steady-state continuous wave photoinduced absorption (cw-PIA) measurements of the $MAPbI_3$ film (see the "Experimental Methods" section in the Supporting Information for details) show clear evidence for the generation of long-lived photoexcited states (with typical lifetimes of the order of milliseconds). Four regions of interest are identified in the cw-PIA spectrum in Figure 2: a photoinduced absorption region between 500−2500 cm^{-1} containing two absorption peaks (region I), a vibrational mode region at 3000-3300 cm^{-1} (region II), a second photoinduced absorption region containing a broad (P_n) transition at ∼6000−11 500 cm^{-1} (region III), and a high-energy modulation region just below the band gap, featuring photoinduced absorption (PA) and photobleaching (PB) (region IV). The concomitant disappearance of P_1, P_2, and P_n at room temperature indicates their common origin (see Figure S3 in the Supporting Information).

Figure 3a show details of the PIA spectrum in region I, featuring two photoinduced absorption bands centered at ∼516 cm^{-1} (P_0) and 1650 cm^{-1} (P_1), as determined by Gaussian fitting curves shown in red, and a series of small features at 620 , 908, 1254, 1460, and 1570 cm^{-1} (solid black lines running across Figures 3a−c and 3d−f) that correspond to the amplitude modulation of the main IR active vibrational (IRAV) modes.[55] An exception is the photoinduced mode at 600 cm^{-1} (within the range of C−N vibrational modes of the organic moiety), which corresponds to an IR inactive Raman mode; this suggests breaking of the inversion symmetry that governs mutually exclusive Raman and IR mode selection rules due to the local distortion of the lattice in the presence of the self-trapped charge.[55]

Density functional theory (DFT) calculations accurately account for the experimental observations in region I of the spectrum. The broad PA band P_1 at 1650 cm^{-1} (0.204 eV) corresponds to a convolution of electronic transitions from negative and positive polaron states at $P_e = 0.187$ eV below the CBM and $P_h = 0.235$ eV above the VBM, respectively. Conversely, the P_0 peak centered at 516 cm^{-1} (0.06 eV), that does not emerge from the calculations, is likely due to a trap state.[25] Figures 3e and 3f show the calculated IR and Raman spectra, which correspond to the experimental modes assigned to the organic moiety. The photoinduced modulation of the IRAV modes from 750 cm^{-1} to 2000 cm^{-1} is reproduced reasonably well by the calculations. Figure 3d shows the spectrum obtained by computing the difference between the spectra calculated in the undistorted (Figure 3e) and distorted perovskite lattices. The modulation sign is in agreement with the experiment for each mode, accounting for amplitude increase or decrease of the vibrational transitions upon polaron formation. Notably, this suggests that negative PA dips are due to a decrease of the vibrational transition oscillator strength, rather than to Fano resonances due to quantum interference of electronic and vibrational transitions.[56]

The orthorhombic-phase $MAPbI_3$ shows several IR peaks in the spectral region of 3000−3300 cm^{-1}, which can be assigned to both C−H and N−H stretching modes of the organic cations. The photoinduced modulation of these modes in region II is particularly interesting (Figure 4). We fitted the experimental PA data in this region to its first and second derivative (Figure 4a). The first derivative component of the absorption spectrum gives an indication of the spectral blue shift of the peak, while the second derivative component is related to the peak broadening.[57] Both effects can be attributed to the modulation of C−H and N−H bonds induced by the

DOI: 10.1021/acsmaterialslett.9b00276
ACS Materials Lett. 2020, 2, 20−27

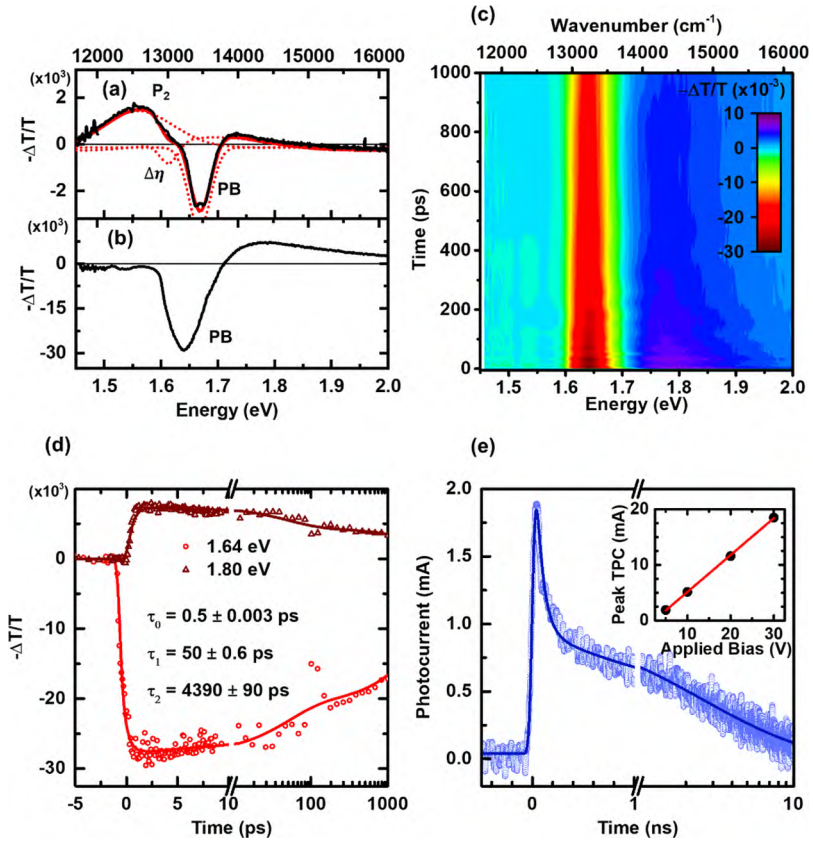

Figure 5. Ultrafast polaron formation and decay dynamics. (a) Comparison between steady-state (top panel) and t = 1.5 ps transient (bottom panel) photoinduced absorption spectra of $MAPbI_3$. The steady-state spectrum (also shown in Figure 2) was fitted with four Gaussians curves: P_2 centered around 1.55 eV, PB centered around 1.67 eV and the effect of change in refractive index modeled by the sum of two Gaussians centered around 1.61 and 1.69 eV. (b) Two-dimensional (2D) map of transient absorption; global fitting yielded three distinctive lifetimes τ_0 = 0.500 ± 0.003 ps, τ_1 = 50.0 ± 0.6 ps, and τ_2 = 4390 ± 90 ps. (c) Temporal slices of transient absorption at 1.64 and 1.80 eV, displaying similar decay dynamics. (d) Fast transient photocurrent decay obtained with an applied voltage of 5 V; fitting to a biexponential decay yielded distinctive lifetimes of τ_1 = 101 ± 1 ps and τ_2 = 4220 ± 20 ps. The inset shows the linear dependence of the transient photocurrent peak on applied bias. In panels (c) and (d), note the shift in time scale from linear to logarithmic, in correspondence to the scale break.

polaron which, by locally distorting the perovskite lattice, indirectly affect their vibrational potential through the hydrogen bonds between hydrogen atoms of $-NH_3$ and I atoms in charged $MAPbI_3$ (*spectator modes*). Note that thermal modulation cannot account for this effect as it determines an opposite red shift of the mode frequency (mode softening), see the Supporting Information. Despite the slight mismatch of calculated and experimental IR mode frequencies in both neutral and excited states (Figure 4b), the blue shift induced by the lattice distortion on the vibrational modes is correctly reproduced by the calculations. Thus, the observed long-lived vibrational frequency renormalization upon photoexcitation is a clear fingerprint of the generation of a geometrically relaxed state.

The concomitant photoinduced electronic spectrum, with intragap transitions, corroborate the assignment to photogenerated polarons. Details of the cw-PIA spectrum in region IV are shown in the top panel of Figure 5a. The spectrum can be fitted to four Gaussian curves, labelled P_2 (centered at ∼1.55 eV), PB (centered at ∼1.67 eV), and a sum of two Gaussians centered at ∼1.61 eV and ∼1.69 eV to model the effect of the change in refractive index, as reported by Price et al.[58] P_2 corresponds well to the energetics determined for ground state to polaron transitions, while the PB peak is assigned to the valence to conduction band (refer to the energy diagram in Figure 2b).

All steady-state spectroscopy results seem to point to large polarons being the primary photoexcitations in 3D $MAPbI_3$. To determine their generation and relaxation dynamics, we performed ultrafast (fs) transient absorption and fast (ps) transient photocurrent measurements (see Figure 5). The time evolution of the transient photoinduced absorption (TPA) spectrum upon pulsed laser excitation ($t \approx 100$ fs, λ = 400 nm, I = 5 nJ/pulse) is shown in the 2D contour plot in Figure 5b. There are two key features in the TPA spectrum, consisting of a broad absorption peak from 1.7 eV to 2.0 eV (13 700−16 100 cm^{-1}) and a sharp peak centered at 1.64 eV (13 200 cm^{-1}), which corresponds to the ground-state bleaching of $MAPbI_3$. Comparison of the cw-PIA and TPA spectra of $MAPbI_3$ (Figures 5a, top and bottom panels) shows good qualitative agreement, with coexistence of PIA and PB components at different relative positions. The red-shift of the photobleaching peak in cw-PIA, relative to the transient data, is likely due to the change in bandgap from 1.67 eV to 1.64 eV, from the high-temperature tetragonal phase to the low-temperature orthorhombic phase,[59] since cw-PIA was collected at ∼80 K, whereas TPA was obtained at room

DOI: 10.1021/acsmaterialslett.9b00276
ACS Materials Lett. 2020, 2, 20−27

temperature. Moreover, the TA spectrum contains contributions from both neutral excitons and charged polarons.

The correspondence between early-time TPA and cw-PIA spectra indicates that the long-lived polaronic species are generated at an ultrafast time scale (t < 100 fs). From the global fitting of the spectral decays (see representative dynamics in Figure 5c), we determined three distinctive time constants of τ_0 = 0.500 ± 0.003 ps, τ_1 = 50.0 ± 0.6 ps, and τ_2 = 4390 ± 90 ps for sequential exponential decays. We attribute the ultrafast relaxation process of 0.500 ps to lattice thermalization, and we attribute the longer time constants to polaron population decay. The recombination process is far from being completed within our experimental temporal range, suggesting a long-lived polaron population that is consistent with the observation up to the milliseocnd (ms) time domain. Note that transient features between 1.7 eV and 2.0 eV have been previously observed in $MAPbI_3$ films[17,18,60,61] and assigned to band filling effects by Manser et al.,[60] while Zhai et al. ascribed them to the photogeneration of free carriers.[61] The long-lived decay was also determined in an earlier study, but not attributed to specific features.[17]

The picosecond transient photocurrent (TPC) induced by a femtosecond laser pulse in a photoconductive switch was measured by using a new-generation high-speed oscilloscope equipped with a 65 GHz real-time sampling channel (Figure 5d). Unlike all-optical photoinduced absorption measurements that may include signatures of neutral (e.g. excitonic) photogenerated species, fast TPC waveforms provide a direct and selective measurement of charge carrier generation and decay dynamics that immediately correlate with transport characteristics of photovoltaic devices. The fast rise time of the TPC signal (limited by the instrument response function) is consistent with the sub-picosecond polaron generation inferred from TPA measurements. The characteristic photocurrent decay times obtained by a biexponential fit with τ_1 = 101 ± 1 ps and τ_2 = 4220 ± 20 ps also compare well against the long-lived polaron lifetimes observed in transient absorption (τ_1 = 50.0 ± 0.6 ps and τ_2 = 4390 ± 90 ps). Note that the initial dynamics of TPA is likely to include exciton decay, which accounts for its faster early time constant. The inset of Figure 5c shows the linear relation between peak transient photocurrent and applied voltage, which enables the extraction of charge carrier mobility in the linear regime (see the "Experimental Methods" section in the Supporting Information). The resulting early-time polaron mobility is of the order of 10 $cm^2\ V^{-1}\ s^{-1}$. In comparison, the mobility obtained from steady-state photocurrent measurements of the same sample is on the order of μ_{ss} = 0.2−2 $cm^2\ V^{-1}\ s^{-1}$, assuming a long polaron lifetime extending to the 1−10 ms time scale. Early-time (pre-trapping) mobility values are indeed expected to be larger than steady-state mobility values, which are dominated by thermally activated trapping and detrapping,[62] and closer to bandlike mobility estimated by first-principles calculations.[3]

Theory for single-crystal $MAPI_3$ yields the mobility values summarized in Table 1 for both positive and negative polarons in the relevant crystallographic directions. The important outcomes are described as follows:

(i) Polaron mobilities are systematically lower than free carrier mobilities, as expected from the enlarged effective masses associated to the phonon clouds. In the low-temperature phase, polaron mobilities are 3−8 times smaller than free carrier effective masses, whereas in the high-temperature phase, polaron mobilities are 1.3−3 times smaller.
(ii) Mobility anisotropy of polarons is smaller than their effective mass anisotropy.
(iii) Theory compares reasonably well with data in the literature reporting mobilities of perovskite single crystals from 2.5 $cm^2\ V^{-1}\ s^{-1}$ to 600 $cm^2\ V^{-1}\ s^{-1}$.[49,63−66]

Our experimental data were obtained in polycrystalline films and cannot be compared directly to single-crystal data nor theoretical values. In addition, measurements at different time scales provide different effective mobility values. Just on single crystals,[67] reported mobilities vary from almost 1000 to 1 $cm^2\ V^{-1}\ s^{-1}$ going from THz (ps time scale) through microwave reflectivity (μs time scale) to space-charge limited current (ms time scale) experimental techniques. In films, mobilities span 2 orders of magnitude, from 0.1 $cm^2\ V^{-1}\ s^{-1}$ to 80 $cm^2\ V^{-1}\ s^{-1}$. Our results are obtained with complementary techniques not yet reported, and they compare reasonably well with the existing literature data.

In conclusion, we have provided a clear indication that the same type of lattice relaxation known to lead to the photogeneration of small polarons in low-dimensional perovskites also occurs in the 3D metal halide perovskite $MAPbI_3$. However, in the 3D case, topological constraints limit the extent of lattice deformation, because of the balance between the electronic energy and the lattice elastic energy. In this situation, the phonon dressed self-trapped states give rise to large polarons with radius extending over a few lattice sites. Such large polarons are generated at ultrafast time scale and are long-lived, with a fraction of the initial population surviving up to the millisecond (ms) time domain, as we see in cw-PIA spectra that clearly indicate vibrational mode frequency renormalization. Large polarons bring about an increase of the effective carrier mass and a concomitant reduction in mobility, overall preserving a large $\mu\tau$ product. Theory accounts for the geometrical relaxation and the vibrational mode renormalization associated to the polaron state, predicts transport anisotropy, and reproduces the low-energy polaron electronic spectrum seen in cw-PIA. It also predicts a small charge symmetry breaking, yielding ambipolar transport, even in the polaron regime. Carrier recombination is affected by their polaronic nature, for the phonon cloud around the carrier in 3D ionic crystals increases charge screening and reduces Coulomb-mediated interactions. This picture validates the idea that large polarons are responsible for the anomalous transport characteristics of metal halide perovskites, including lowering of carrier mobility via rescaling of the effective mass, protection against carrier scattering, and suppression of bimolecular (Langevin) recombination channels.

■ ASSOCIATED CONTENT

Supporting Information

The Supporting Information is available free of charge at https://pubs.acs.org/doi/10.1021/acsmaterialslett.9b00276.

Materials and methods; computational details; supporting figures and table (PDF)

■ AUTHOR INFORMATION

Corresponding Author

*E-mail: csoci@ntu.edu.sg.

ORCID

Jun Yin: 0000-0002-1749-1120

DOI: 10.1021/acsmaterialslett.9b00276
ACS Materials Lett. 2020, 2, 20−27

Andrew C. Grimsdale: 0000-0003-2498-3024
Omar F. Mohammed: 0000-0001-8500-1130
Guglielmo Lanzani: 0000-0002-2442-4495
Cesare Soci: 0000-0002-0149-9128

Author Contributions

[∇]These authors contributed equally

Notes

The authors declare no competing financial interest.

■ ACKNOWLEDGMENTS

We would like to thank Dr. Zilong Wang for the preliminary transient photocurrent data and assistance from Teledyne LeCroy Application Engineer Mr. Wayne Lim. W.P.D.W. is grateful to Dr. Meng Lee Leek and Dr. Vijila Chellappan for fruitful discussions. Research was supported by the National Research Foundation (No. NRF-CRP14-2014-03), by the Ministry of Education (Nos. MOE2016-T1-1-164 and MOE2018-T1-2-040), and by the Agency for Science, Technology and Research (A*STAR, Award No. A18A7b0058) of Singapore. Work at King Abdullah University of Science and Technology was supported by the KAUST Supercomputing Laboratory.

■ REFERENCES

(1) Jeon, N. J.; Noh, J. H.; Kim, Y. C.; Yang, W. S.; Ryu, S.; Seok, S. I. Solvent Engineering for High-Performance Inorganic-Organic Hybrid Perovskite Solar Cells. *Nat. Mater.* **2014**, *13*, 897−903.
(2) Zhao, Y.; Zhu, K. Solution Chemistry Engineering toward High-Efficiency Perovskite Solar Cells. *J. Phys. Chem. Lett.* **2014**, *5*, 4175−4186.
(3) Chin, X. Y.; Cortecchia, D.; Yin, J.; Bruno, A.; Soci, C. Lead Iodide Perovskite Light-Emitting Field-Effect Transistor. *Nat. Commun.* **2015**, *6*, 7383.
(4) Cho, H.; Jeong, S.-H.; Park, M.-H.; Kim, Y.-H.; Wolf, C.; Lee, C.-L.; Heo, J. H.; Sadhanala, A.; Myoung, N.; Yoo, S.; et al. Overcoming the Electroluminescence Efficiency Limitations of Perovskite Light-Emitting Diodes. *Science* **2015**, *350*, 1222−1225.
(5) Wong, A. B.; Lai, M.; Eaton, S. W.; Yu, Y.; Lin, E.; Dou, L.; Fu, A.; Yang, P. Growth and Anion Exchange Conversion of $CH_3NH_3PbX_3$ Nanorod Arrays for Light-Emitting Diodes. *Nano Lett.* **2015**, *15*, 5519−5524.
(6) Tan, Z.-K.; Moghaddam, R. S.; Lai, M. L.; Docampo, P.; Higler, R.; Deschler, F.; Price, M.; Sadhanala, A.; Pazos, L. M.; Credgington, D.; et al. Bright Light-Emitting Diodes Based on Organometal Halide Perovskite. *Nat. Nanotechnol.* **2014**, *9*, 687−692.
(7) Zhu, H.; Fu, Y.; Meng, F.; Wu, X.; Gong, Z.; Ding, Q.; Gustafsson, M. V.; Trinh, M. T.; Jin, S.; Zhu, X. Y. Lead Halide Perovskite Nanowire Lasers with Low Lasing Thresholds and High Quality Factors. *Nat. Mater.* **2015**, *14*, 636−642.
(8) Sutherland, B. R.; Hoogland, S.; Adachi, M. M.; Wong, C. T. O.; Sargent, E. H. Conformal Organohalide Perovskites Enable Lasing on Spherical Resonators. *ACS Nano* **2014**, *8*, 10947−10952.
(9) Xing, G.; Mathews, N.; Lim, S. S.; Yantara, N.; Liu, X.; Sabba, D.; Grätzel, M.; Mhaisalkar, S.; Sum, T. C. Low-Temperature Solution-Processed Wavelength-Tunable Perovskites for Lasing. *Nat. Mater.* **2014**, *13*, 476.
(10) Cadelano, M.; Sarritzu, V.; Sestu, N.; Marongiu, D.; Chen, F.; Piras, R.; Corpino, R.; Carbonaro, C. M.; Quochi, F.; Saba, M.; et al. Can Trihalide Lead Perovskites Support Continuous Wave Lasing? *Adv. Opt. Mater.* **2015**, *3*, 1557−1564.
(11) Yuan, F.; Wu, Z.; Dong, H.; Xia, B.; Xi, J.; Ning, S.; Ma, L.; Hou, X. Electric Field-Modulated Amplified Spontaneous Emission in Organo-Lead Halide Perovskite $CH_3NH_3PbI_3$. *Appl. Phys. Lett.* **2015**, *107*, 261106.
(12) Neutzner, S.; Srimath Kandada, A. R.; Lanzani, G.; Petrozza, A. A Dual-Phase Architecture for Efficient Amplified Spontaneous Emission in Lead Iodide Perovskites. *J. Mater. Chem. C* **2016**, *4*, 4630−4633.
(13) Gratzel, M. The Light and Shade of Perovskite Solar Cells. *Nat. Mater.* **2014**, *13*, 838−842.
(14) Filippetti, A.; Caddeo, C.; Delugas, P.; Mattoni, A. Appealing Perspectives of Hybrid Lead−Iodide Perovskites as Thermoelectric Materials. *J. Phys. Chem. C* **2016**, *120*, 28472−28479.
(15) Chen, W.; Bhaumik, S.; Veldhuis, S. A.; Xing, G.; Xu, Q.; Grätzel, M.; Mhaisalkar, S.; Mathews, N.; Sum, T. C. Giant Five-Photon Absorption from Multidimensional Core-Shell Halide Perovskite Colloidal Nanocrystals. *Nat. Commun.* **2017**, *8*, 15198.
(16) Brenner, T. M.; Egger, D. A.; Kronik, L.; Hodes, G.; Cahen, D. Hybrid Organic-Inorganic Perovskites: Low-Cost Semiconductors with Intriguing Charge-Transport Properties. *Nat. Rev. Mater.* **2016**, *1*, 15007.
(17) Stranks, S. D.; Eperon, G. E.; Grancini, G.; Menelaou, C.; Alcocer, M. J. P.; Leijtens, T.; Herz, L. M.; Petrozza, A.; Snaith, H. J. Electron-Hole Diffusion Lengths Exceeding 1 Micrometer in an Organometal Trihalide Perovskite Absorber. *Science* **2013**, *342*, 341−344.
(18) Xing, G.; Mathews, N.; Sun, S.; Lim, S. S.; Lam, Y. M.; Grätzel, M.; Mhaisalkar, S.; Sum, T. C. Long-Range Balanced Electron- and Hole-Transport Lengths in Organic-Inorganic $CH_3NH_3PbI_3$. *Science* **2013**, *342*, 344−347.
(19) Wehrenfennig, C.; Liu, M.; Snaith, H. J.; Johnston, M. B.; Herz, L. M. Charge-Carrier Dynamics in Vapour-Deposited Films of the Organolead Halide Perovskite $CH_3NH_3PbI_{3-x}Cl_x$. *Energy Environ. Sci.* **2014**, *7*, 2269−2275.
(20) Savenije, T. J.; Ponseca, C. S.; Kunneman, L.; Abdellah, M.; Zheng, K.; Tian, Y.; Zhu, Q.; Canton, S. E.; Scheblykin, I. G.; Pullerits, T.; et al. Thermally Activated Exciton Dissociation and Recombination Control the Carrier Dynamics in Organometal Halide Perovskite. *J. Phys. Chem. Lett.* **2014**, *5*, 2189−2194.
(21) Green, M. A.; Ho-Baillie, A.; Snaith, H. J. The Emergence of Perovskite Solar Cells. *Nat. Photonics* **2014**, *8*, 506−514.
(22) Yin, W.-J.; Shi, T.; Yan, Y. Unusual Defect Physics in $CH_3NH_3PbI_3$ Perovskite Solar Cell Absorber. *Appl. Phys. Lett.* **2014**, *104*, 063903.
(23) Brandt, R. E.; Stevanović, V.; Ginley, D. S.; Buonassisi, T. Identifying Defect-Tolerant Semiconductors with High Minority-Carrier Lifetimes: Beyond Hybrid Lead Halide Perovskites. *MRS Commun.* **2015**, *5*, 265−275.
(24) Alarousu, E.; El-Zohry, A. M.; Yin, J.; Zhumekenov, A. A.; Yang, C.; Alhabshi, E.; Gereige, I.; AlSaggaf, A.; Malko, A. V.; Bakr, O. M.; et al. Ultralong Radiative States in Hybrid Perovskite Crystals: Compositions for Submillimeter Diffusion Lengths. *J. Phys. Chem. Lett.* **2017**, *8*, 4386−4390.
(25) De Angelis, F.; Petrozza, A. Clues from Defect Photochemistry. *Nat. Mater.* **2018**, *17*, 383−384.
(26) Maynard, B.; Long, Q.; Schiff, E. A.; Yang, M.; Zhu, K.; Kottokkaran, R.; Abbas, H.; Dalal, V. L. Electron and Hole Drift Mobility Measurements on Methylammonium Lead Iodide Perovskite Solar Cells. *Appl. Phys. Lett.* **2016**, *108*, 173505.
(27) Wehrenfennig, C.; Eperon, G. E.; Johnston, M. B.; Snaith, H. J.; Herz, L. M. High Charge Carrier Mobilities and Lifetimes in Organolead Trihalide Perovskites. *Adv. Mater.* **2014**, *26*, 1584−1589.
(28) Ahn, N.; Son, D.-Y.; Jang, I.-H.; Kang, S. M.; Choi, M.; Park, N.-G. Highly Reproducible Perovskite Solar Cells with Average Efficiency of 18.3% and Best Efficiency of 19.7% Fabricated Via Lewis Base Adduct of Lead(II) Iodide. *J. Am. Chem. Soc.* **2015**, *137*, 8696−8699.
(29) Stoumpos, C. C.; Malliakas, C. D.; Kanatzidis, M. G. Semiconducting Tin and Lead Iodide Perovskites with Organic Cations: Phase Transitions, High Mobilities, and near-Infrared Photoluminescent Properties. *Inorg. Chem.* **2013**, *52*, 9019−9038.
(30) Chen, Y.; Peng, J.; Su, D.; Chen, X.; Liang, Z. Efficient and Balanced Charge Transport Revealed in Planar Perovskite Solar Cells. *ACS Appl. Mater. Interfaces* **2015**, *7*, 4471−4475.

DOI: 10.1021/acsmaterialslett.9b00276
ACS Materials Lett. 2020, 2, 20−27

(31) Ghosh, T.; Aharon, S.; Etgar, L.; Ruhman, S. Free Carrier Emergence and Onset of Electron−Phonon Coupling in Methylammonium Lead Halide Perovskite Films. *J. Am. Chem. Soc.* **2017**, *139*, 18262−18270.
(32) Miyata, K.; Meggiolaro, D.; Trinh, M. T.; Joshi, P. P.; Mosconi, E.; Jones, S. C.; De Angelis, F.; Zhu, X.-Y. Large Polarons in Lead Halide Perovskites. *Sci. Adv.* **2017**, *3*, No. e1701217.
(33) Zhu, X. Y.; Podzorov, V. Charge Carriers in Hybrid Organic−Inorganic Lead Halide Perovskites Might Be Protected as Large Polarons. *J. Phys. Chem. Lett.* **2015**, *6*, 4758−4761.
(34) Cortecchia, D.; Yin, J.; Bruno, A.; Lo, S.-Z. A.; Gurzadyan, G. G.; Mhaisalkar, S.; Bredas, J.-L.; Soci, C. Polaron Self-Localization in White-Light Emitting Hybrid Perovskites. *J. Mater. Chem. C* **2017**, *5*, 2771−2780.
(35) Yin, J.; Li, H.; Cortecchia, D.; Soci, C.; Brédas, J.-L. Excitonic and Polaronic Properties of 2d Hybrid Organic−Inorganic Perovskites. *ACS Energy Lett.* **2017**, *2*, 417−423.
(36) Cortecchia, D.; Neutzner, S.; Srimath Kandada, A. R.; Mosconi, E.; Meggiolaro, D.; De Angelis, F.; Soci, C.; Petrozza, A. Broadband Emission in Two-Dimensional Hybrid Perovskites: The Role of Structural Deformation. *J. Am. Chem. Soc.* **2017**, *139*, 39−42.
(37) Smith, M. D.; Karunadasa, H. I. White-Light Emission from Layered Halide Perovskites. *Acc. Chem. Res.* **2018**, *51*, 619−627.
(38) Lin, H.; Zhou, C.; Tian, Y.; Siegrist, T.; Ma, B. Low-Dimensional Organometal Halide Perovskites. *ACS Energy Lett.* **2018**, *3*, 54−62.
(39) Cortecchia, D.; Yin, J.; Petrozza, A.; Soci, C. White Light Emission in Low-Dimensional Perovskites. *J. Mater. Chem. C* **2019**, *7*, 4956−4969.
(40) Thouin, F.; Valverde-Chávez, D. A.; Quarti, C.; Cortecchia, D.; Bargigia, I.; Beljonne, D.; Petrozza, A.; Silva, C.; Srimath Kandada, A. R. Phonon Coherences Reveal the Polaronic Character of Excitons in Two-Dimensional Lead Halide Perovskites. *Nat. Mater.* **2019**, *18*, 349−356.
(41) Neutzner, S.; Thouin, F.; Cortecchia, D.; Petrozza, A.; Silva, C.; Srimath Kandada, A. R. Exciton-Polaron Spectral Structures in Two Dimensional Hybrid Lead-Halide Perovskites. *Phys. Rev. Mater.* **2018**, *2*, 064605.
(42) Emin, D. Optical Properties of Large and Small Polarons and Bipolarons. *Phys. Rev. B: Condens. Matter Mater. Phys.* **1993**, *48*, 13691−13702.
(43) Emin, D. Large-Polaron Transport. In *Polarons*; Emin, D., Ed.; Cambridge University Press: Cambridge, U.K., 2012; pp 86−94.
(44) Fu, J.; Xu, Q.; Han, G.; Wu, B.; Huan, C. H. A.; Leek, M. L.; Sum, T. C. Hot Carrier Cooling Mechanisms in Halide Perovskites. *Nat. Commun.* **2017**, *8*, 1300.
(45) Slonopas, A.; Foley, B. J.; Choi, J. J.; Gupta, M. C. Charge Transport in Bulk $CH_3NH_3PbI_3$ Perovskite. *J. Appl. Phys.* **2016**, *119*, 074101.
(46) Yang, X.; Wang, Y.; Li, H.; Sheng, C. Optical Properties of Heterojunction between Hybrid Halide Perovskite and Charge Transport Materials: Exciplex Emission and Large Polaron. *J. Phys. Chem. C* **2016**, *120*, 23299−23303.
(47) Ivanovska, T.; Dionigi, C.; Mosconi, E.; De Angelis, F.; Liscio, F.; Morandi, V.; Ruani, G. Long-Lived Photoinduced Polarons in Organohalide Perovskites. *J. Phys. Chem. Lett.* **2017**, *8*, 3081−3086.
(48) La-o-vorakiat, C.; Xia, H.; Kadro, J.; Salim, T.; Zhao, D.; Ahmed, T.; Lam, Y. M.; Zhu, J.-X.; Marcus, R. A.; Michel-Beyerle, M.-E.; et al. Phonon Mode Transformation across the Orthohombic−Tetragonal Phase Transition in a Lead Iodide Perovskite $CH_3NH_3PbI_3$: A Terahertz Time-Domain Spectroscopy Approach. *J. Phys. Chem. Lett.* **2016**, *7*, 1−6.
(49) Valverde-Chavez, D. A.; Ponseca, C. S.; Stoumpos, C. C.; Yartsev, A.; Kanatzidis, M. G.; Sundstrom, V.; Cooke, D. G. Intrinsic Femtosecond Charge Generation Dynamics in Single Crystal $CH_3NH_3PbI_3$. *Energy Environ. Sci.* **2015**, *8*, 3700−3707.
(50) Zheng, K.; Abdellah, M.; Zhu, Q.; Kong, Q.; Jennings, G.; Kurtz, C. A.; Messing, M. E.; Niu, Y.; Gosztola, D. J.; Al-Marri, M. J.; et al. Direct Experimental Evidence for Photoinduced Strong-Coupling Polarons in Organolead Halide Perovskite Nanoparticles. *J. Phys. Chem. Lett.* **2016**, *7*, 4535−4539.
(51) Zhu, H.; Miyata, K.; Fu, Y.; Wang, J.; Joshi, P. P.; Niesner, D.; Williams, K. W.; Jin, S.; Zhu, X.-Y. Screening in Crystalline Liquids Protects Energetic Carriers in Hybrid Perovskites. *Science* **2016**, *353*, 1409−1413.
(52) Batignani, G.; Fumero, G.; Srimath Kandada, A. R.; Cerullo, G.; Gandini, M.; Ferrante, C.; Petrozza, A.; Scopigno, T. Probing Femtosecond Lattice Displacement Upon Photo-Carrier Generation in Lead Halide Perovskite. *Nat. Commun.* **2018**, *9*, 1971.
(53) Park, M.; Neukirch, A. J.; Reyes-Lillo, S. E.; Lai, M.; Ellis, S. R.; Dietze, D.; Neaton, J. B.; Yang, P.; Tretiak, S.; Mathies, R. A. Excited-State Vibrational Dynamics toward the Polaron in Methylammonium Lead Iodide Perovskite. *Nat. Commun.* **2018**, *9*, 2525.
(54) Tsai, H. H.; Nie, W. Y.; Blancon, J. C.; Stoumpos, C. C. S.; Asadpour, R.; Harutyunyan, B.; Neukirch, A. J.; Verduzco, R.; Crochet, J. J.; Tretiak, S.; et al. High-Efficiency Two-Dimensional Ruddlesden-Popper Perovskite Solar Cells. *Nature* **2016**, *536*, 312−316.
(55) Miranda, P. B.; Moses, D.; Heeger, A. J. Ultrafast Photogeneration of Charged Polarons in Conjugated Polymers. *Phys. Rev. B: Condens. Matter Mater. Phys.* **2001**, *64*, 081201.
(56) Narra, S.; Chung, C.-C.; Diau, E. W.-G.; Shigeto, S. Simultaneous Observation of an Intraband Transition and Distinct Transient Species in the Infrared Region for Perovskite Solar Cells. *J. Phys. Chem. Lett.* **2016**, *7*, 2450−2455.
(57) Lanzani, G. *The Photophysics Behind Photovoltaics and Photonics*; John Wiley & Sons: Chichester, U.K., 2012.
(58) Price, M. B.; Butkus, J.; Jellicoe, T. C.; Sadhanala, A.; Briane, A.; Halpert, J. E.; Broch, K.; Hodgkiss, J. M.; Friend, R. H.; Deschler, F. Hot-Carrier Cooling and Photoinduced Refractive Index Changes in Organic−Inorganic Lead Halide Perovskites. *Nat. Commun.* **2015**, *6*, 8420.
(59) Kong, W.; Ye, Z.; Qi, Z.; Zhang, B.; Wang, M.; Rahimi-Iman, A.; Wu, H. Characterization of an Abnormal Photoluminescence Behavior Upon Crystal-Phase Transition of Perovskite $CH_3NH_3PbI_3$. *Phys. Chem. Chem. Phys.* **2015**, *17*, 16405−16411.
(60) Manser, J. S.; Kamat, P. V. Band Filling with Free Charge Carriers in Organometal Halide Perovskites. *Nat. Photonics* **2014**, *8*, 737−743.
(61) Zhai, Y.; Sheng, C. X.; Zhang, C.; Vardeny, Z. V. Ultrafast Spectroscopy of Photoexcitations in Organometal Trihalide Perovskites. *Adv. Funct. Mater.* **2016**, *26*, 1617−1627.
(62) Moses, D.; Soci, C.; Chi, X.; Ramirez, A. P. Mechanism of Carrier Photogeneration and Carrier Transport in Molecular Crystal Tetracene. *Phys. Rev. Lett.* **2006**, *97*, 067401.
(63) Wehrenfennig, C.; Eperon, G. E.; Johnston, M. B.; Snaith, H. J.; Herz, L. M. High Charge Carrier Mobilities and Lifetimes in Organolead Trihalide Perovskites. *Adv. Mater.* **2014**, *26*, 1584−1589.
(64) Saidaminov, M. I.; Abdelhady, A. L.; Murali, B.; Alarousu, E.; Burlakov, V. M.; Peng, W.; Dursun, I.; Wang, L.; He, Y.; Maculan, G.; et al. High-Quality Bulk Hybrid Perovskite Single Crystals within Minutes by Inverse Temperature Crystallization. *Nat. Commun.* **2015**, *6*, 7586.
(65) Dong, Q.; Fang, Y.; Shao, Y.; Mulligan, P.; Qiu, J.; Cao, L.; Huang, J. Electron-Hole Diffusion Lengths > 175 μm in Solution-Grown $CH_3NH_3PbI_3$ Single Crystals. *Science* **2015**, *347*, 967−970.
(66) Shi, D.; Adinolfi, V.; Comin, R.; Yuan, M.; Alarousu, E.; Buin, A.; Chen, Y.; Hoogland, S.; Rothenberger, A.; Katsiev, K.; et al. Low Trap-State Density and Long Carrier Diffusion in Organolead Trihalide Perovskite Single Crystals. *Science* **2015**, *347*, 519.
(67) Herz, L. M. Charge-Carrier Mobilities in Metal Halide Perovskites: Fundamental Mechanisms and Limits. *ACS Energy Lett.* **2017**, *2*, 1539−1548.

DOI: 10.1021/acsmaterialslett.9b00276
ACS Materials Lett. 2020, 2, 20−27